NASA Contractor Report 172170

ICASE

SPECTRAL METHODS FOR INVISCID, COMPRESSIBLE FLOWS

(NASA-CR-172710) SPECTRAL METHODS FOR INVISCID, COMPRESSIBLE FLOWS Final Report (NASA) 40 p HC A03/MF A01 CSCL 01A

N83-33847

Unclas
G3/02 36104

M. Y. Hussaini

M. D. Salas

T. A. Zang

Contract No. NAS1-16394, NAS1-17130
July 1983

INSTITUTE FOR COMPUTER APPLICATIONS IN SCIENCE AND ENGINEERING
NASA Langley Research Center, Hampton, Virginia 23665

Operated by the Universities Space Research Association

NASA
National Aeronautics and
Space Administration

Langley Research Center
Hampton, Virginia 23665

SPECTRAL METHODS FOR INVISCID, COMPRESSIBLE FLOWS

M. Y. Hussaini
Institute for Computer Applications in Science and Engineering

M. D. Salas
NASA Langley Research Center

T. A. Zang
NASA Langley Research Center

ABSTRACT

Recent developments in the application of spectral methods to two-dimensional compressible flows are reviewed. A brief introduction to spectral methods — their history and especially their implementation — is provided. The stress is on those techniques relevant to transonic flow computation. The spectral multigrid iterative methods are discussed with application to the transonic full potential equation. Discontinuous solutions of the Euler equations are considered. The key element is the shock fitting technique which is briefly explained.

Research of the first author was supported by the National Aeronautics and Space Administration under NASA Contract Nos. NAS1-16394 and NAS1-17130 while he was in residence at ICASE, NASA Langley Research Center, Hampton, VA 23665. The work of the third author was supported by NASA Grant No. NAG1-109 while he was at the College of William and Mary, Williamsburg, VA 23185.

1. INTRODUCTION

Spectral methods have their roots in approximation theory. They are based on representations of the solution to a problem by a finite series of global (and preferably orthogonal) functions. The expansion coefficients are usually referred to as spectra, and hence this technique is called the spectral method. All the derivatives of the solution are approximated by the corresponding derivatives of the finite series expansion. Under the right circumstances such high-order approximations can produce extremely accurate numerical solutions. There are three versions of spectral methods: spectral Galerkin, spectral tau, and spectral collocation. An extended discussion of each of these versions is given in [1].

The first serious application of spectral methods to fluid dynamics used the Galerkin approach: the solution was expanded in a series of functions satisfying the boundary conditions and the calculation was performed entirely in terms of the expansion coefficients. Already in 1954 Silberman [2] used them for meteorological modelling. The numerous investigations which followed Silberman's work established the feasibility of the spectral method for low resolution calculations. In particular, Ellsaesser [3] showed that for the simple balanced barotropic model the efficiency of a low resolution spectral method was competitive with the then available low resolution finite difference methods. However, the cost of these early spectral Galerkin methods soared to a prohibitive level as the number of expansion functions (and hence the resolution) increased. The high cost was due to the straightforward manner in which the convolution sums arising from the nonlinear terms were evaluated.

The breakthrough came when Orszag [4], [5] (and also Eliasen, et al. [6]) proposed a transform method for handling the convolution sums. This change so improved the efficiency of spectral methods that they became practical for high-resolution calculations, even in three dimensions. Indeed, the accuracy of spectral Galerkin methods is so great, especially in terms of their extremely favorable phase errors, that they are now routinely used in numerical weather prediction. They have also been profitably applied to the simulation of homogeneous, isotropic turbulence [7].

The spectral tau method was devised by Lanczos [8]. Its principal difference from the spectral Galerkin method lies in the treatment of boundary conditions. Lanczos used Chebyshev polynomials as the expansion functions for solving linear ordinary differential equations with rational coefficients. Orszag [9], [10] has applied this method to certain fluid dynamics problems.

For many problems, especially nonlinear ones, the spectral collocation method is the easiest to implement as well as the most efficient. The earliest investigations of this method are those of Kreiss and Oliger [11], (who called it the Fourier method) and Orszag [6], [12] (who termed it pseudospectral). Thus far this has been the only type of spectral method yet applied to transonic problems. The present discussion will be confined to spectral collocation methods, with all future references to spectral methods implicitly referring to this specific type.

Spectral calculations of compressible flows have only been performed in the last few years. The initial investigations were for one-dimensional flows. These were carried out by Zang and Hussaini [13], Gottlieb, et al. [14], and Taylor, et al. [15]. Some promising two-dimensional transonic results have been obtained recently for the full potential equation by Streett [16] and Streett, et al [17] and for the Euler equations by Salas, et al. [18] and Hussaini, et al. [19]. This article will describe the details of the spectral methods employed in these two-dimensional calculations and will present some representative results. Since spectral methods are a novel approach to transonic flow computations, a basic introduction to their properties and implementation will be presented first.

2. FUNDAMENTALS OF SPECTRAL METHODS

For problems with periodic boundary conditions spectral methods based upon Fourier series are the obvious choice. If the boundary conditions are Dirichlet or Neumann, then Chebyshev polynomials are usually employed. For many problems an appropriate spectral method can produce a rapidly convergent approximation. The particular choices mentioned above have the added advantage of efficient implementation via the Fast Fourier Transform. This section will furnish the details necessary for implementing these spectral methods. To begin with, however, the convergence properties of spectral methods will be illustrated with two elementary examples. The first of these has some of the characteristics of the steady potential calculations described in Section 4, whereas the second is relevant to the time-dependent Euler solutions of Section 5.

2.1. A One-dimensional Elliptic Problem

A major reason for the appeal of spectral methods is their potential for rapidly convergent approximations. The Fourier series expansion over $[0,2\pi]$ of the function

$$u(x) = \frac{3}{5 - 4\cos x} \tag{1}$$

provides a simple illustration. It is

$$u(x) = \sum_{k=-\infty}^{\infty} \tilde{u}_k e^{ikx}, \tag{2}$$

where

$$\tilde{u}_k = 2^{-|k|}. \tag{3}$$

The approximation obtained by truncating the Fourier series,

$$u_N(x) = \sum_{k=-N/2+1}^{N/2-1} \tilde{u}_k e^{ikx}, \tag{4}$$

satisfies

$$|u_N(x) - u(x)| \leq 4e^{-(\frac{\ell n\, 2}{2})N} . \tag{5}$$

It converges exponentially fast, i.e.,

$$N^p |u_N(x) - u(x)| \to 0 \quad \text{as} \quad N \to \infty \tag{6}$$

for all positive integers p. This property of exponential convergence is exhibited by the truncated Fourier series of any periodic function which is infinitely differentiable. The rapid decay of the Fourier series of such a function follows from repeated integrations-by-parts: Let $u(x)$ be periodic and infinitely differentiable on $[0,2\pi]$. Its Fourier coefficients are given by

$$\tilde{u}_k = \frac{1}{2\pi} \int_0^{2\pi} u(x) e^{-ikx} dx. \tag{7}$$

A single integration-by-parts yields

$$\tilde{u}_k = \frac{1}{(-ik)} e^{-ikx} u(x) \Big|_0^{2\pi} + \frac{1}{(ik)} \int_0^{2\pi} u'(x) e^{-ikx} dx. \tag{8}$$

The boundary term vanishes because of the periodicity requirement. The remaining integral is $o(1)$ as $k \to \infty$ by the Riemann-Lebesque Lemma because of the differentiability condition. Thus, a single integration lets us conclude that $\tilde{u}_k = o(k^{-1})$. Clearly, p integrations produce $\tilde{u}_k = o(k^{-p})$. Note that both the periodicity and differentiability conditions are necessary for this argument. If either fails, then the rate of convergence is algebraic.

A Fourier spectral method for a differential equation makes use of some finite Fourier series representation of the solution. This series will be related to, but different from, the truncated Fourier series of Eq. (4). The details are furnished in Section 2.3. Consider the differential equation

$$\frac{d^2u}{dx^2} - u = f \tag{9}$$

on $[0,2\pi]$ with periodic boundary conditions. Suppose that f is chosen so that the exact solution is given by Eq (1). Applied to this problem the spectral method yields the results shown in the third column of Table I. The second column gives the results of the truncated Fourier series and the last column reports the results for a second-order finite difference method. Note that the bound given by Eq. (5) for the truncated Fourier series is sharp -- the entries in the second column agree precisely with this bound until N is so large that round-off error predominates. (These calculations were performed on a CDC Cyber-175, which has 14 significant digits.) The correct $N = 128$ and $N = 256$ entries are 2.17(-19) and 1.18(-38), respectively. The exponential convergence of the truncated Fourier series is evident. The spectral method performs nearly as well. (In fact, its maximum error for $N = 32$ and $N = 64$ is considerably lower, but this is due to a cancellation of error. In an RMS sense these two respective truncated series and Fourier spectral errors are within several percent.) Only at very low resolution is the spectral method substantially worse than the truncated series. But, of course, the major point of this example is the decided superiority of the spectral method over the second-order finite difference approximation.

Table I. Maximum Error for a 1-D Periodic Problem

N	Truncated Series	Fourier Spectral	Finite Difference
4	1.00 (0)	4.42 (0)	6.28 (0)
8	2.50 (-1)	1.28 (0)	1.98 (0)
16	1.56 (-2)	3.15 (-2)	2.02 (-1)
32	6.10 (-5)	3.46 (-5)	3.61 (-2)
64	9.31 (-10)	4.89 (-10)	8.65 (-3)
128	5.68 (-14)	7.11 (-14)	2.14 (-3)
256	5.68 (-14)	7.11 (-14)	5.34 (-4)

R.

2.2. A One-dimensional Hyperbolic Problem

Spectral methods for time-dependent problems can also exhibit exponential convergence. Indeed, spectral methods have thus far made a greater impact on evolution equations than on steady-state ones. A simple example is provided by the wave equation

$$\frac{\partial u}{\partial t} + \frac{\partial u}{\partial x} = 0 \tag{10}$$

on the interval $[-1,1]$ with initial condition $u(x,0)$ and boundary condition $u(-1,t)$. Since this is not a periodic problem, a spectral method based upon Fourier series in x would exhibit extremely slow convergence: the Fourier coefficients decay only as fast as $O(k^{-1})$ in the general case. (The integration-by-parts argument given earlier fails, even if the solution is infinitely differentiable because the boundary term in Eq. (8) is finite.) However, rapid convergence as well as efficient algorithms can be attained for spectral methods based upon Chebyshev polynomials. These are defined on $[-1,1]$ by

$$T_n(x) = \cos\,(n \cos^{-1} x). \tag{11}$$

The function

$$u(x,t) = \sin \alpha\pi(x-t) \tag{12}$$

is one solution to Eq. (10). It has the Chebyshev expansion

$$u(x,t) = \sum_{n=0}^{\infty} \tilde{u}_n(t)\, T_n(x), \tag{13}$$

where

$$\tilde{u}_n(t) = \frac{2}{c_n} \sin\left(\frac{n\pi}{2} - \alpha\pi t\right) J_n(\alpha\pi) \tag{14}$$

with

$$c_n = \begin{matrix} 2 & n = 0 \\ 1 & n \geq 1 \end{matrix} \tag{15}$$

and $J_n(t)$ is the Bessel function of order n. The asymptotic properties of the Bessel functions imply that

$$n^p \tilde{u}_n(t) \to 0 \qquad \text{as} \quad n \to \infty \tag{16}$$

for all positive integers p. Note that this result holds whether or not α is an integer. In contrast, the Fourier coefficients of $u(x,t)$ are

$$\tilde{u}_k(t) = \frac{i}{2\pi} e^{i\alpha\pi t} \frac{\sin \pi(\alpha+k)}{\alpha+k} - \frac{i}{2\pi} e^{-i\alpha\pi t} \frac{\sin \pi(\alpha-k)}{\alpha-k} . \tag{17}$$

For non-integer α these decay extremely slowly.

The change of variables

$$x = \cos\theta, \tag{18}$$

the definition

$$v(\theta,t) = u(\cos\theta,t), \tag{19}$$

and Eq. (11) reduce Eq. (13) to

$$v(\theta,t) = \sum_{n=0}^{\infty} \tilde{u}_n(t) \cos n\theta. \tag{20}$$

Thus, the Chebyshev coefficients of $u(x,t)$ are precisely the Fourier coefficients of $v(\theta,t)$. This new function is automatically periodic. If $u(x,t)$ is infinitely differentiable (in x), then $v(\theta,t)$ will be infinitely differentiable (in θ). Hence, straightforward integration-by-parts arguments lead to the conclusion that the Chebyshev coefficients of an infinitely differentiable function will decay exponentially fast. Note that this holds regardless of the boundary conditions.

The effectiveness of this type of approximation is demonstrated by the results in Table II. Shown there are the errors at $t = 1$ for several approximations to Eq. (10) with initial and boundary conditions based on Eq. (12) for $\alpha = 2.5$.

(The explicit time-step used in these calculations has been taken to be so small that time-discretization errors, but not round-off errors, are negligible.) The results of a spectral method based on Fourier series have been included to emphasize the importance of the proper choice of expansion functions.

Table II. Maximum Error for a 1-D Hyperbolic Problem

N	Truncated Series	Chebyshev Spectral	Fourier Spectral	Finite Difference
4	1.24 (0)	1.49 (0)	1.85 (0)	1.64 (0)
8	1.25 (-1)	6.92 (-1)	1.92 (0)	1.73 (0)
16	7.03 (-6)	1.50 (-4)	2.27 (0)	1.23 (0)
32	1.62 (-13)	3.45 (-11)	2.28 (0)	3.34 (-1)
64	1.79 (-13)	9.55 (-11)	2.27 (0)	8.44 (-2)

2.3. Implementation of Fourier Spectral Methods

The key to the implementation of Fourier spectral methods is the Discrete Fourier Transform. Let a function $u(x)$ be represented by its values $u_j = u(x_j)$ at the collocation points

$$x_j = \frac{2\pi j}{N} \qquad j = 0,1,\cdots,N-1. \tag{21}$$

The discrete Fourier coefficients of u_j are

$$\hat{u}_k = \frac{1}{N}\sum_{j=0}^{N-1} u_j e^{-ikx_j} \qquad k = -\frac{N}{2}, -\frac{N}{2}+1,\cdots,\frac{N}{2}-1. \tag{22}$$

The inverse relationship is

$$u_j = \sum_{k=-N/2}^{N/2-1} \hat{u}_k e^{ikx_j} \qquad j = 0,1,\cdots,N-1, \tag{23}$$

and the orthogonality relation is

$$\frac{1}{N}\sum_{j=0}^{N-1} e^{ikx_j} = \hat{\delta}_{k,0}\ , \tag{24}$$

where

$$\hat{\delta}_{k,\ell} = \begin{cases} 1 & k = \ell,\ \ell\pm N,\ \ell\pm 2N,\cdots \\ 0 & \text{otherwise} \end{cases}. \tag{25}$$

Note the difference between Eq. (24) and the orthogonality relation for continuous Fourier series. In the latter case the sum is replaced by an integral and the usual Kronecker delta function appears on the right-hand side.

The counterpart of the periodicity condition $u(x+2\pi) = u(x)$ is

$$u_{j+N} = u_j. \tag{26}$$

Unlike the continuous case, discrete Fourier series also have a periodicity requirement on the coefficients:

$$\hat{u}_{k+N} = \hat{u}_k. \tag{27}$$

This is an immediate consequence of Eq. (22). The connection between the discrete and continuous Fourier coefficients follows from Eqs. (2), (22), and (24) and is

$$\hat{u}_k = \sum_{\ell=-\infty}^{\infty} \tilde{u}_{k+\ell N}. \tag{28}$$

All but the $\ell = 0$ contribution to the sum are the aliases of $\tilde{u}_k$, i.e., Fourier components which are indistinguishable from $\tilde{u}_k$ on the discrete grid. These are a source of error in spectral methods in addition to the error that arises from the truncation of the exact Fourier series. It is just such aliasing terms that account for the differences between the entries in columns 2 and 3 of Table I.

Here then are the details of the spectral method used for the Table I results:

1) Given $f_j = f(x_j)$ for $j = 0,1,\cdots,N-1$, find the discrete Fourier coefficients $\hat{f}_k$ for $k = -N/2, -N/2+1,\cdots,N/2-1$. (Use Eq. (22) with f in place of u.)

2) Set

$$\hat{u}_k = \begin{cases} -\dfrac{\hat{f}_k}{1+k^2} & |k| < N/2 \\ 0 & k = -N/2 \end{cases}. \tag{29}$$

(This is the solution of Eq. (9) in terms of the Fourier coefficients.)

3) Compute u_j itself for $j = 0,1,\cdots,N-1$ from its discrete Fourier coefficients. (Use Eq. (23).)

The Fast Fourier Transform (FFT) is an efficient and widely-available algorithm (even in assembly language) for accomplishing steps (1) and (3). A broad survey of FFT's is provided in [20]. The only slight complication is that standard versions of the FFT (such as the IMSL subroutine FFT2) produce the coefficients for $k = 0,1,\cdots,N-1$. The periodicity relation given by Eq. (27) enables the desired coefficients to be extracted readily from the FFT output. The periodicity relation also helps in using the FFT to perform sums such as those in Eq. (23).

The ease with which a direct solution is attainable for this spectral discretization of Eq. (9) is exceptional. For example, no efficient direct solution scheme exists for the spectral solution of

$$\frac{\partial}{\partial x}\left(a(x,y)\,\frac{\partial u}{\partial x}\right) + \frac{\partial}{\partial y}\left(b(x,y)\,\frac{\partial u}{\partial y}\right) = f. \tag{30}$$

One must, in general, resort to iterative schemes for its solution. An essential element of these schemes is the explicit evaluation of terms such as those appearing in Eq. (30). Consider just the first term. Given $u(x,y)$ at the collocation points, this term is evaluated by

1) computing $\partial u/\partial x$ by Fourier collocation,
2) multiplying by $a(x,y)$, and
3) computing $\partial/\partial x\left(a(x,y)\partial u/\partial x\right)$ by Fourier collocation.

The differentiation occurring in step 1 involves (with the y-dependence suppressed):

(i) using the FFT to compute the discrete Fourier coefficients $\hat{u}_k$ for $k = -N/2,-N/2+1,\cdots,N/2-1$,

(ii) setting

$$\hat{v}_k = \begin{cases} ik\hat{u}_k & |k| < \frac{N}{2} \\ 0 & k = -\frac{N}{2} \end{cases}, \tag{31}$$

(iii) using the (inverse) FFT on $\hat{v}_k$ to get $\partial u/\partial x$ at the collocation points.

The choice of $\hat{v}_{-N/2}$ calls for some explanation. Since $u(x)$ is real, so too will be $\hat{u}_{-N/2}$. But only the real part of $\hat{v}_{-N/2}$ makes any effective contribution to $\partial u/\partial x$. If a derivative of higher-order is desired, then steps (i) to (iii) still apply but with the appropriate power of ik appearing as the multiplier of $\hat{u}_k$ in Eq. (31).

The FFT enables the left-hand side of Eq. (30) to be evaluated at all the $N \times N$ collocation points in $O(N^2 \ln N)$ operations. For large N this compares unfavorably with the finite difference cost of $O(N^2)$ for an $N \times N$ grid. However, when judged by the cost of equally accurate solutions the spectral method is likely to be cheaper since it needs a coarser grid (see Table I).

2.4. Implementation of Chebyshev Spectral Methods

A Chebyshev spectral method makes use of a finite Chebyshev series such as

$$u_N(x) = \sum_{n=0}^{N} \hat{u}_n T_n(x). \tag{32}$$

The standard collocation points are

$$x_j = \cos \frac{\pi j}{N} \qquad j = 0, 1, \cdots, N. \tag{33}$$

Thus,

$$u_j = \sum_{n=0}^{N} \hat{u}_n \cos \frac{n\pi j}{N}, \tag{34}$$

where u_j is the approximation to $u(x_j)$. The inverse relation is

$$\hat{u}_n = \frac{2}{N\bar{c}_n} \sum_{j=0}^{N} \bar{c}_j^{-1} u_j \cos \frac{n\pi j}{N}, \tag{35}$$

where

$$\bar{c}_j = \begin{cases} 2 & j = 0 \text{ or } N \\ 1 & 1 \leq j \leq N-1 \end{cases}. \tag{36}$$

These last two sums may be evaluated by the FFT. The standard FFT, however, does complex arithmetic and ignores the symmetry present in a cosine transform. The second appendix of [6] describes how to make more efficient use of the FFT for evaluating the sums in Eqs. (34) and (35). One may also use a Fast Cosine Transform. A Fortran listing of one version is given in [21].

The Chebyshev collocation points are the extreme points of $T_N(x)$. Note that they are not evenly distributed in x, but rather are clustered near the endpoints. The smallest mesh size scales as $1/N^2$. While this distribution contributes to the quality of the Chebyshev approximation and permits the use of the FFT in evaluating the series, it also places a severe time-step limitation on explicit methods for evolution equations.

A Chebyshev spectral method for Eq. (10) combines some explicit time-discretization with an approximation to the spatial derivative which is based upon analytical differentiation of the Chebyshev series for u. Consider first the infinite series, for which

$$u(x) = \sum_{n=0}^{\infty} \tilde{u}_n T_n(x), \tag{37}$$

with the time dependence of u suppressed. Write the expansion of the derivative as

$$u'(x) = \sum_{n=0}^{\infty} \tilde{u}_n^{(1)} T_n(x). \tag{38}$$

The goal is to relate the coefficients in Eqs. (37) and (38). The starting point is the recursion relation

$$\frac{T'_{n+1}(x)}{n+1} - \frac{T'_{n-1}(x)}{n-1} = \frac{2}{c_n} T_n(x), \tag{39}$$

which follows from Eq. (11). Inserted into Eq. (38) this produces

$$\begin{aligned} u'(x) &= \tfrac{1}{2} \sum_{n=0}^{\infty} c_n \tilde{u}_n^{(1)} \left[\frac{T'_{n+1}(x)}{n+1} - \frac{T'_{n-1}(x)}{n-1}\right] \\ &= \sum_{n=1}^{\infty} \frac{c_{n-1}\tilde{u}_{n-1}^{(1)}}{2n} T'_n(x) - \sum_{n=1}^{\infty} \frac{\tilde{u}_{n+1}^{(1)}}{2n} T'_n(x). \end{aligned} \tag{40}$$

But from Eq. (37)

$$u'(x) = \sum_{n=1}^{\infty} \tilde{u}_n T'_n(x). \tag{41}$$

Therefore,

$$2n\, \tilde{u}_n = c_{n-1}\tilde{u}_{n-1}^{(1)} - \tilde{u}_{n+1}^{(1)} \qquad n \geq 1. \tag{42}$$

The evaluation of the $\partial u/\partial x$ term in the Chebyshev spectral method for Eq. (10) consists of:

1) Given $u_j = u(x_j)$ for $j = 0,1,\cdots,N$ find the discrete Chebyshev coefficients $\hat{u}_n$ for $n = 0,1,\cdots,N$. (Use Eq. (35).)

2) Set

$$\hat{u}_{N+1}^{(1)} = 0,$$
$$\hat{u}_{N}^{(1)} = 0, \tag{43}$$

and compute $\hat{u}_n^{(1)}$ for $n = N-1, N-2, \cdots, 0$ from

$$c_n \hat{u}_n^{(1)} = \hat{u}_{n+2}^{(1)} + 2(n+1)\hat{u}_{n+1}. \tag{44}$$

3) Compute $\partial u/\partial x(x_j)$ itself for $j = 0,1,\cdots,N$ from its discrete Chebyshev coefficients. (Use the analog of Eq. (34).)

Higher-order derivatives can be calculated by repeating step (2) as often as needed. When the FFT is used for steps (1) and (3) the cost of a derivative evaluation is $O(N \ln N)$.

For the Eq. (10) calculation, the derivative $\partial u/\partial x$ is not needed at the inflow boundary $(x = -1)$ since the boundary condition rather than the PDE is used to update u_N. Note that there is no need for a special formula at the outflow boundary $(x = +1)$. Although the PDE is used to update u_0, the value of $\partial u/\partial x$ at $x = 1$ is automatically available from the Chebyshev spectral calculation outlined above. In contrast the second-order finite difference calculation used for Table II employed the special formula of first-order extrapolation at the outflow boundary.

As a general rule the correct numerical boundary conditions for a spectral method are the same as the correct analytical boundary conditions. The global nature of the approximation avoids the need for special differentiation formulae at boundaries. At the same time spectral methods are quite unforgiving of incorrect boundary conditions. The inherent dissipation of these methods is so low that boundary errors quickly contaminate the entire solution. In many fluid dynamical applications the computational region must be terminated at some finite, artificial boundary. The difficulty at "artificial" boundaries is that analytically correct, fully nonlinear boundary conditions for systems are seldom known. One example of a workable artificial boundary condition for the Euler equations is given in Section 5.4.

3. SPECTRAL MULTIGRID ITERATIVE METHODS

Direct solutions of implicit spectral equations -- whether arising from elliptic problems or from implicit time-discretizations of evolution problems -- are rarely feasible.

Except in special cases the matrices representing spectral apfroximations are full. Iterative methods are a practical alternative because the requisite matrix-vector products can be evaluated via the FFT.

3.1. An Elementary Example

An attractive iterative scheme for spectral equations utilizes multigrid concepts. The basic description of spectral multigrid methods for linear, elliptic equations is given in [22] and [23]. Additional considerations for the nonlinear, potential flow application are given in [17]. A brief summary of these concepts is given here since they play a major role in the spectral transonic potential flow calculations discussed in the following section.

The fundamentals of spectral multigrid are perhaps easiest to grasp for the simple model problem

$$- \frac{d^2u}{dx^2} = f \tag{45}$$

on $[0,2\pi]$ with periodic boundary conditions. The Fourier approximation to the left-hand side of Eq. (45) at the collocation points is

$$\sum_{p=-N/2+1}^{N/2-1} p^2 \hat{u}_p e^{ipx_j} . \tag{46}$$

The spectral approximation to Eq. (45) may be expressed as

$$LU = F, \tag{47}$$

where

$$U = (u_0, u_1, \cdots, u_{N-1}), \tag{48}$$

$$F = (f_0, f_1, \cdots, f_{N-1}), \tag{49}$$

and L represents the Fourier spectral approximation to $- d^2/dx^2$.

A Richardson's iterative scheme for solving Eq. (47) is

$$V \leftarrow V + \omega(F - LV), \tag{50}$$

where ω is a relaxation parameter, on the right side of the replacement symbol ($\leftarrow$) V represents the current approximation to U, and on the left it represents the updated approximation. The eigenfunctions of L are

$$\xi_j(p) = e^{2\pi i j p/N}, \tag{51}$$

with the corresponding eigenvalues

$$\lambda(p) = p^2, \tag{52}$$

where $j = 0,1,\cdots,N-1$ and $p = -N/2+1,\cdots,N/2-1$. The index p has a natural interpretation as the frequency of the eigenfunction.

The error at any stage of the iterative process is $V - U$; it can be resolved into an expansion in the eigenvectors of L. Each iteration reduces the p'th error component to $\nu(\lambda_p)$ times its previous value, where

$$\nu(\lambda) = 1 - \omega\lambda. \tag{53}$$

The optimal choice of ω results from minimizing $|\nu(\lambda)|$ for $\lambda \in [\lambda_{min}, \lambda_{max}]$, where $\lambda_{min} = 1$ and $\lambda_{max} = N^2/4$. (One need not worry about the $p = 0$ eigenfunction since it corresponds to the mean level of the solution, which is at one's disposal for this problem.) The optimal relaxation parameter for this single-grid procedure is

$$\omega_{SG} = \frac{2}{\lambda_{max} + \lambda_{min}} . \tag{54}$$

It produces the spectral radius

$$\rho_{SG} = \frac{\lambda_{max} - \lambda_{min}}{\lambda_{max} + \lambda_{min}} . \tag{55}$$

Unfortunately, $\rho_{SG} \simeq 1 - 8/N^2$, which implies that $O(N^2)$ iterations are required to achieve convergence.

This slow convergence is the outcome of balancing the damping of the lowest-frequency eigenfunction with that of the highest-frequency one in the minimax problem described after Eq. (53). The multigrid approach takes advantage of the fact that the low-frequency modes ($|p| < N/4$) can be represented just as well on coarser grids. It settles for balancing the middle-frequency eigenfunction ($|p| = N/4$) with the highest-frequency one ($|p| = N/2$), and hence damps effectively only those modes which cannot be resolved on coarser grids. In Eqs. (54) and (55), λ_{min} is replaced with $\lambda_{mid} = \lambda(N/4)$. The optimal relaxation parameter in this context is

$$\omega_{MG} = \frac{2}{\lambda_{max} + \lambda_{mid}} . \tag{56}$$

The multigrid smoothing factor

$$\mu_{MG} = \frac{\lambda_{max} - \lambda_{mid}}{\lambda_{max} + \lambda_{mid}} \tag{57}$$

measures the damping rate of the high-frequency modes. In this example $\mu_{MG} = 0.60$, independent of N. The price of this effective damping of the high-frequency errors is that the low-frequency errors are hardly damped at all. However, on a grid with $N/2$ collocation points, the modes for $|p| \in [N/8, N/4]$ are now the high-frequency ones. They get damped on this grid. Still coarser grids can be used until relaxations are so cheap that one can afford to damp all the remaining modes, or even to solve the discrete equations exactly.

Let us consider just the interplay between two grids. A general, nonlinear fine-grid problem can be written

$$L^f(U^f) = F^f. \tag{58}$$

The shift to the coarse grid occurs after the fine-grid approximation V^f has been sufficiently smoothed by the relaxation process, i.e., after the high-frequency content of the error $V^f - U^f$ has been sufficiently reduced. The related coarse-grid problem is

$$L^c(U^c) = F^c, \tag{59}$$

where

$$F^c = R\left[F^f - L^f(V^f)\right] + L^c(RV^f). \tag{60}$$

The restriction operator R interpolates a function from the fine grid to the coarse grid. The coarse-grid operator and solution are denoted by L^c and U^c, respectively. After an adequate approximation V^c to the coarse-grid problem has been obtained, the fine-grid approximation is corrected via

$$V^f \leftarrow V^f + P(V^c - RV^f). \tag{61}$$

The prolongation operator P interpolates a function from the coarse grid to the fine grid.

3.2. Interpolation Operators

The spectral multigrid interpolation operators for periodic coordinates amount to trigonometric interpolation: for example, given a function on a coarse grid, compute the discrete Fourier coefficients and then use the resulting discrete Fourier series to construct the interpolated function on the fine grid. This may be accomplished by performing two FFT's. Interpolation for non-periodic coordinates employs Chebyshev series in an analogous fashion. Detailed descriptions of the interpolation operators are available in [17] and [23].

3.3. Coarse-Grid Operator

A typical term in the class of problems containing potential flow is

$$\frac{d}{dx}\left[a(u,x)\,\frac{du}{dx}\right]. \tag{62}$$

The discrete operator which represents its fine-grid spectral approximation is

$$L^f = D\;A\;D, \tag{63}$$

where D is a spectral first-derivative operator (either Fourier or Chebyshev) and A is the diagonal matrix

$$A_{jk} = a(u_j,x_j)\,\delta_{j,k}. \tag{64}$$

Many multigrid investigators have advocated choosing the coarse-grid operator so that

$$L^c = RL^fP. \tag{65}$$

Both the Fourier and the Chebyshev first-derivative operators satisfy

$$D^c = RD^fP. \tag{66}$$

However, Eq. (65) itself is not satisfied if the coarse-grid analog of Eq. (63) is used to define L^c, except in the trivial case for which $a(u,x)$ is a constant. On the other hand, much of the efficiency of the pseudospectral method is lost if Eq. (65) is used to define the coarse-grid operator. The most satisfactory compromise seems to be using Eq. (63) but with the restricted values of $a(u_j,x_j)$ in place of the pointwise values.

4. THE COMPRESSIBLE POTENTIAL EQUATION

The computational results of the past decade have demonstrated that fairly accurate predictions for a number of transonic flows of practical interest can be made on the basis of the compressible potential equation. This nonlinear equation is of mixed elliptic-hyperbolic type, precluding purely elliptic or purely hyperbolic solution procedures. The numerical solution of the potential equation became feasible only after the introduction of type-dependent differencing by Murman and Cole [24]. The review by Hall [25] provides an exhaustive history of computational approaches to the potential equation.

Until the recent work of Streett [16], the discretization procedures for the potential equation were invariably based on low-order finite difference or finite element methods. Streett used a spectral discretization of the full potential equation and obtained its solution by a single-grid iterative technique. The application of spectral multigrid techniques by Streett, et al. [17] produced a dramatic acceleration of the iterative scheme. Even in its relatively primitive state the spectral multigrid scheme is competitive, and in some cases unequivocally more efficient, than standard finite difference schemes.

4.1. The Reduced Potential Problem

Streett solved the two-dimensional full potential equation (applying boundary conditions at the actual airfoil surface). In this work a numerical conformal mapping (also generated by Fourier techniques) was used to transform the airfoil onto the unit circle. Moreover, the calculations were actually performed in terms of the reduced potential G, which is defined by

$$G = \Phi - (R + \frac{1}{R}) \cos \Theta - E \tan^{-1}[\sqrt{1 - M_\infty^2} \tan \Theta], \qquad (67)$$

where Φ is the potential, R and Θ are the computational polar coordinates, E is the circulation and M_∞ is the Mach number at infinity. The reduced potential is periodic in Θ and it satisfies

$$\frac{\partial}{\partial R}\left(R\rho\,\frac{\partial G}{\partial R}\right) + \frac{\partial}{\partial \Theta}\left(\frac{\rho}{R}\,\frac{\partial G}{\partial \Theta}\right) = 0, \tag{68}$$

along with

$$\frac{\partial G}{\partial R} = 0 \qquad \text{at} \quad R = 1, \tag{69}$$

$$G \to 0 \qquad \text{as} \quad R \to \infty, \tag{70}$$

and the Kutta condition. The density is given by the isentropic relation

$$\rho = \left[1 - \frac{\gamma-1}{2} M_\infty^2 (q_r^2 + q_\theta^2 - 1)\right]^{\frac{1}{\gamma-1}}; \tag{71}$$

the ratio of specific heats is denoted by γ, the velocity components in the physical (r,θ) plane are

$$q_r = \frac{1}{H}\,\frac{\partial \Phi}{\partial R} \tag{72}$$

$$q_\theta = \frac{1}{RH}\,\frac{\partial \Phi}{\partial \Theta}\,, \tag{73}$$

and the Jacobian between the complex physical plane $(z = re^{i\theta})$ and the complex computational plane $(\sigma = Re^{i\Theta})$ is

$$H = \left|\frac{dz}{d\sigma}\right|. \tag{74}$$

4.2. Discretization

The spectral method employs a Fourier series representation in Θ. Constant grid spacing in Θ corresponds to a convenient dense spacing in the physical plane at the leading and trailing edges. The domain in R (with a large, but finite outer cutoff) is mapped onto the standard Chebyshev domain $[-1,1]$ by an analytical stretching transformation that clusters the collocation points near the airfoil surface. The stretching is so severe that the ratio of the largest-to-smallest radial intervals is typically greater than 1000.

The most expedient technique for dealing with the mixed elliptic-hyperbolic nature of the transonic problem is to use the artificial density approach of Hafez, et al. [26]. The original artificial density is

$$\tilde{\rho} = \rho - \mu \overset{+}{\delta} \rho \tag{75}$$

with

$$\mu = \max\{0, 1 - \frac{1}{M^2}\}, \tag{76}$$

where M is the local Mach number and $\overleftarrow{\delta}\rho$ is an upwind first-order (undivided) difference. The spectral calculations employed a higher-order artificial density formula. The spectral method also required a weak filtering technique to deal with some high-frequency oscillations generated by the shock. Details are available in [16].

4.3. Spectral Multigrid Solution Scheme

Let the spectral discretization of Eqs. (68) - (70) be denoted by

$$M(U) = 0, \tag{77}$$

and define

$$J(U) = \frac{\partial M}{\partial U}(U). \tag{78}$$

A suitable relaxation scheme for the spectral multigrid solution of transonic potential flow is based upon approximate factorization techniques similar to those used in finite difference discretizations [27]. The Jacobian $J(U)$ is split into the sum of two operators $J_x(U)$ and $J_y(U)$, each involving derivatives in only the one coordinate direction indicated by the subscript. The most straightforward spectral approximate factorization scheme is

$$[\alpha I - J_x(V)][\alpha I - J_y(V)]\Delta V = \omega\alpha M(V), \tag{79}$$

where V is the last estimate of U, and $V + \Delta V$ is the next estimate. This is commonly referred to as AF1 for the transonic problem. For second-order spatial discretizations the term $[\alpha I - J_x(V)]$ leads to a set of tridiagonal systems, one for each value of y. The second left-hand side factor produces another set of tridiagonal systems. For spectral discretizations, however, these systems are full; hence, Eq. (79) is still relatively expensive to invert. The spectral factorization scheme makes the additional approximation of replacing J_x and J_y with their second-order finite difference analogs, denoted by H_x and H_y, respectively:

$$[\alpha I - H_x(V)][\alpha I - H_y(V)]\Delta V = \omega\alpha M(V). \tag{80}$$

For purely finite difference approximations some analytical results are available for selecting optimal values for the parameters α and ω [28]. No similar results are yet available for the spectral approximation. By analogy with the finite difference case ω was chosen to be of order unity and a sequence of α's was selected in a range $[\alpha_\ell,\alpha_h]$ by the rule

$$\alpha^k = \alpha_h\left(\frac{\alpha_\ell}{\alpha_h}\right)^{\frac{k-1}{K-1}}, \tag{81}$$

where K denotes the number of distinct α's. The choices of α_ℓ and α_h were based in part on estimates of the eigenvalue range of the discrete operators and in (much greater) part by trial and error. Fortunately, the AF1 scheme is not very sensitive to these parameters. This basic iterative scheme may be employed in either a single-grid or a multigrid context. In the latter case the parameters α_ℓ and α_h should be chosen separately for each grid to optimize the high-frequency damping.

The spectral multigrid solutions of Streett, et al., used three different fine grids (with the coarser levels in parentheses): 16 × 32 (12 × 16 and 8 × 8), 16 × 48 (14 × 32, 12 × 16 and 8 × 8) and 18 × 64 (16 × 48, 14 × 32, 12 × 16 and 8 × 8). Note that in passing to a coarser level the grid is typically reduced by less than a factor of 2 in each coordinate direction. This choice leads to a significant improvement over the standard gridding for the spectral potential flow problem, especially in the supercritical regime where the solution has large high-frequency content.

All the spectral multigrid results were obtained with the same fixed schedule: start on the finest grid, work down to the coarsest grid and then back up to the finest grid; on the way down there is 1 sweep though the (three) parameter sequence and on the way up there are 2 sweeps.

4.4. Airfoil Examples

The flow past an NACA 0012 airfoil at 4^o angle of attack and a freestream Mach number of 0.5 is a challenging subcritical case. The airfoil produces a fairly large lift coefficient at these conditions and the surface pressure distribution shows a sharp suction peak near the leading edge. Since the local Mach number in this peak is nearly 1, compressibility effects are substantial.

Nevertheless, the spectral solution on a relatively coarse grid captures all the essential details of the flow. The surface pressure coefficient from the spectral code MGAFSP [17] using 16 points in the radial (R) direction, and 32 points in the azimuthal (Θ) direction is displayed in Fig. 1.

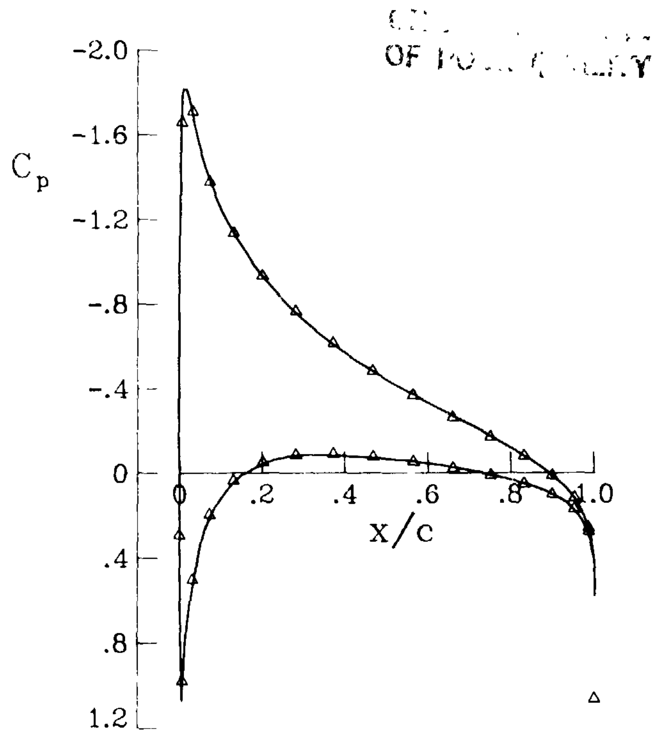

Figure 1. Spectral (triangles) and finite difference (solid line) surface pressures for a subcritical flow.

The symbols denote the solution at the collocation points. For comparison, the result from the finite difference, multigrid, approximate factorization code FLO36 [29] is shown as a solid line. The grid used in the benchmark finite difference calculation is so fine (64 × 384 points) that the truncation error is well below plotting accuracy. The FLO36 and MGAFSP results are identical to plotting accuracy. The spectral computation on this mesh yields a lift coefficient with truncation error less than 10^{-4}. Spectral solutions on a 16 × 32 grid are thus of more than adequate resolution and accuracy for subcritical flows.

In Figure 2 are shown convergence histories from FLO36, MGAFSP, and the finite difference, approximate factorization, single-grid code TAIR [27]. Meshes which yield approximately equivalent accuracy were chosen. The surface pressure results are the same to plotting accuracy, the lift coefficient is converged in the third decimal place, and the predicted drag coefficient is less than .001. (Actually, the spectral result is an order of magnitude more accurate than these limits, but the TAIR result barely meets them.)

A lifting supercritical case is provided by the NACA 0012 airfoil at $M_\infty = 0.75$ and $\alpha = 2^o$. This yields a section lift coefficient of nearly 0.6. A shock appears only on the upper surface for these conditions and is rather strong for a potential calculation; the normal Mach number ahead of the

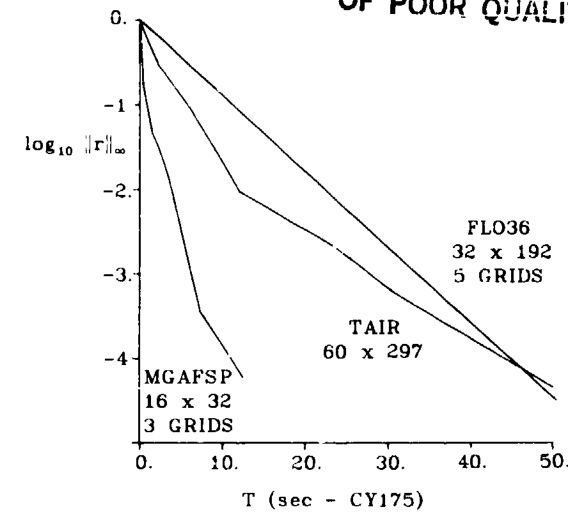

Figure 2. Maximum residual versus machine time for a subcritical flow.

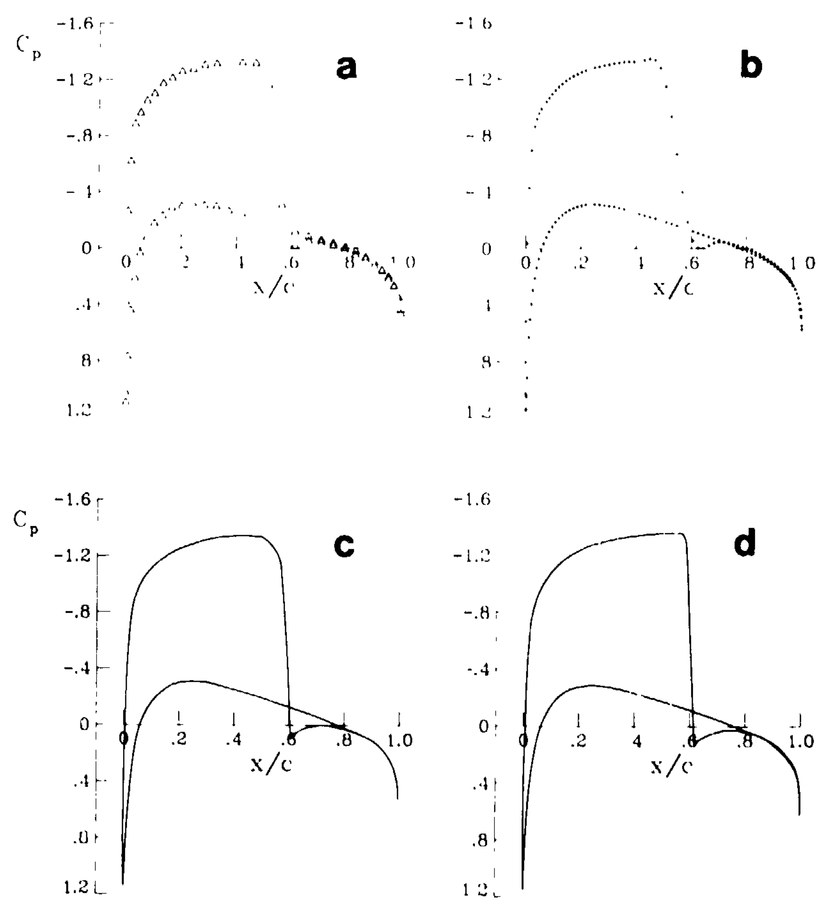

Figure 3. Surface pressures for a supercritical flow:
a) MGAFSP at collocation points; b) MGAFSP interpolated onto finer grid; c) TAIR, and d) FLO36.

shock is about 1.36. Lifting supercritical cases are especially difficult for spectral methods since the solution will always have significant content in the entire frequency spectrum: the shock populates the highest frequencies of the grid and the lift is predominantly on the scale of the entire domain. An iterative scheme therefore must be able to damp error components across the spectrum.

Surface pressure distributions from MGAFSP, TAIR, and FLO36 are shown in Figure 3. The respective computational grids are 18 × 64, 30 × 149, and 32 × 192. The latter two are the default grids for the production finite difference codes. Spectral results obtained by trigonometrically interpolating the 18 × 64 grid results onto a much finer grid are included alongside the results at the collocation points. This reveals the wealth of detail that is provided by the rather coarse spectral grid. The shock predicted by TAIR is far more rounded and smeared than that of FLO36, reflecting the coarser mesh and larger artificial viscosity used in the former. The TAIR result shown is also only correct to one decimal place in lift as compared with a finer-grid result. Convergence histories for these three cases are shown in Figure 4 along with the results for MGAFSP on a coarser grid (16 × 48).

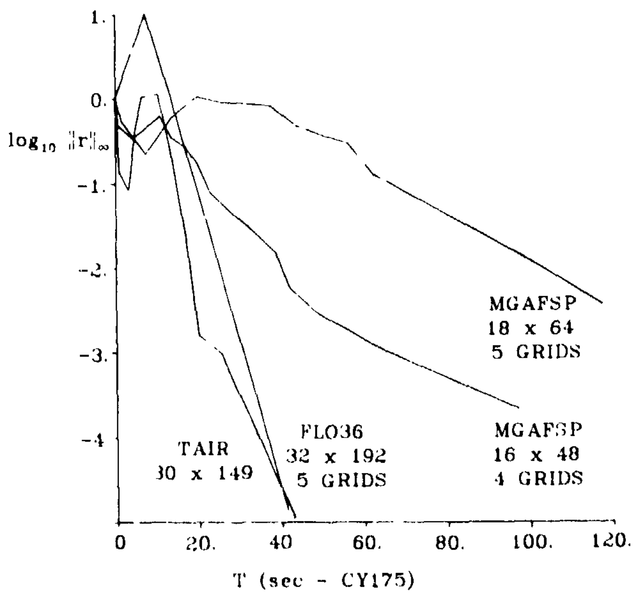

Figure 4. Maximum residual versus machine time for a supercritical flow.

5. THE EULER EQUATIONS

The Euler equations undoubtedly provide more information than the potential flow approximation. The numerical difficulties in solving the Euler equations are well known. The problems tend to be even more severe with spectral than finite difference methods. Explicit time-stepping schemes are especially costly because the Chebyshev collocation points have a very small spacing near the boundary. The numerical boundary conditions, particularly for artificial boundaries, must be sophisticated because spectral methods are extremely sensitive to improper boundary treatments. The oscillations arising in shock-capturing methods are quite troublesome because the global nature of spectral approximations spreads the oscillations over the entire domain.

Spectral methods for compressible flows are still so novel that most of these difficulties remain to be surmounted. However, at least the shock-induced oscillations can be avoided by resorting to shock-fitting techniques. Here the shock front is a computational boundary whose shape and motion are generated during the calculation. Since the flow within the computational domain is smooth, there is reason to expect a shock-fitted solution to be highly accurate. Shock-fitted spectral solutions to the Euler equations were first presented by Salas, et al. [18]. Results for related problems were subsequently given by Zang, et al. [30]. Additional examples and more numerical details are contained in [19]. The essential features of these investigations follow.

5.1. The Shock Interaction Problem

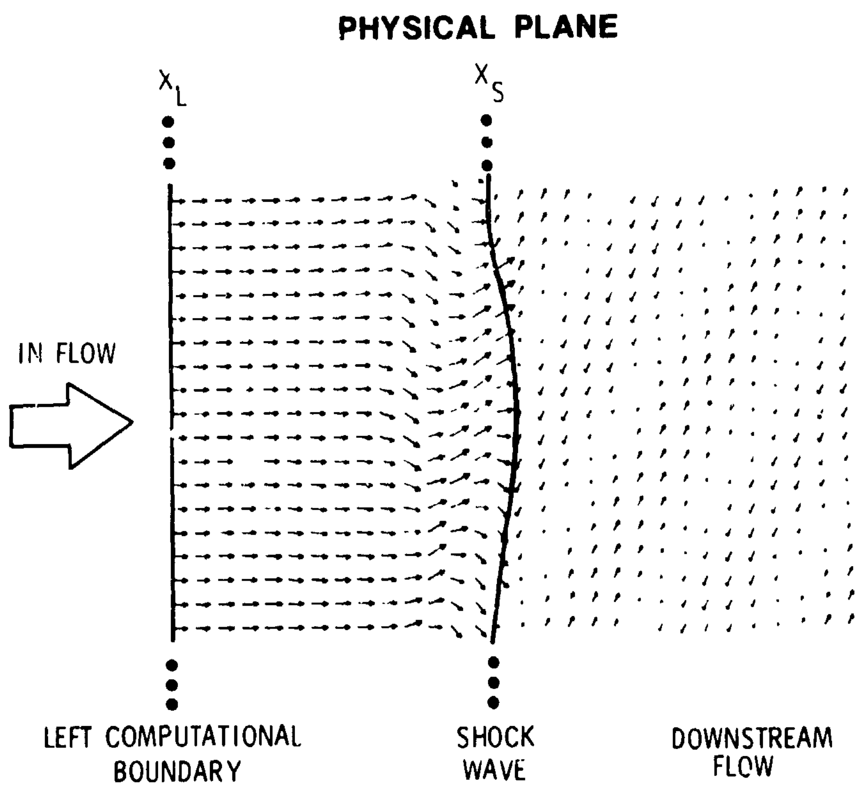

Figure 5. Model problem in the physical domain a short time after the start of the calculation.

A model problem which has been used to study the interaction of a shock wave with a vortex [31] or with idealized turbulence [32] is illustrated in Figure 5. At time $t = 0$ an infinite, normal shock at $x = 0$ separates a rapidly moving, uniform fluid on the left from the fluid on the right which is in a quiescent state except for some specified fluctuation. The initial conditions are chosen so that in the absence of any fluctuation the shock moves uniformly in the positive x-direction with a Mach number (relative to the fluid on the right) denoted by M_s. In the presence of fluctuations the shock front will develop ripples. The shape of the shock is described by the function $x_s(y,t)$. The numerical calculations are used to determine the state of the fluid in the region between the shock front and some suitable left boundary $x_L(t)$ and also to determine the motion and shape of the shock front itself.

The physical domain in which the fluid motion is computed is given by

$$\begin{aligned} &x_L(t) < x < x_s(y,t) \\ &-\infty < y < \infty \qquad\qquad (82) \\ &t > 0. \end{aligned}$$

The change of variables

$$\begin{aligned} X &= \frac{x - x_L(t)}{x_s(y,t) - x_L(t)} \\ Y &= \frac{1}{2}\left[1 + \tanh(\alpha y)\right] \qquad\qquad (83) \\ T &= t, \end{aligned}$$

produces the computational domain

$$\begin{aligned} &0 < X < 1 \\ &0 < Y < 1 \qquad\qquad (84) \\ &T > 0. \end{aligned}$$

The stretching parameter α is typical of order 1.

The fluid motion is modeled by the two-dimensional Euler equations. In terms of the computational coordinates these are

$$Q_T + B\, Q_X + C\, Q_Y = 0, \tag{85}$$

where

$$Q = [P, u, v, S], \tag{86}$$

$$B = \begin{bmatrix} U & \gamma X_x & \gamma X_y & 0 \\ \frac{a^2}{\gamma} X_x & U & 0 & 0 \\ \frac{a^2}{\gamma} X_y & 0 & U & 0 \\ 0 & 0 & 0 & U \end{bmatrix}, \tag{87}$$

and

$$C = \begin{bmatrix} V & \gamma Y_x & \gamma Y_y & 0 \\ \frac{a^2}{\gamma} Y_x & V & 0 & 0 \\ \frac{a^2}{\gamma} Y_y & 0 & V & 0 \\ 0 & 0 & 0 & V \end{bmatrix}. \tag{88}$$

The contravariant velocity components are given by

$$U = X_t + uX_x + vX_y$$

and

$$V = Y_t + uY_x + vY_y. \tag{89}$$

A subscript denotes partial differentiation with respect to the indicated variable. P, a, and S are the natural logarithm of pressure, the sound speed, and the entropy (divided by the specific heat at constant volume), respectively, all normalized by reference conditions at downstream infinity; u and v are velocity components in the x- and y-directions, both scaled by the characteristic velocity defined by the square root of the pressure-density ratio at downstream infinity. A value $\gamma = 1.4$ has been used.

5.2. Discretization

Let k denote the time level and let Δt be the time-step increment. The time discretization of Eq. (85) is then as follows:

$$\tilde{Q} = [1 - \Delta t L^k] Q^k, \tag{90}$$

$$Q^{k+1} = \tfrac{1}{2}\left[Q^k + (1 - \Delta t\tilde{L})\tilde{Q}\right], \tag{91}$$

where the spatial operator L represents an approximation to $B\,\partial/\partial X + C\,\partial/\partial Y$. In the spectral method, the solution Q is first expanded as a double Chebyshev series,

$$Q(X,Y,T) = \sum_{p=0}^{M}\sum_{q=0}^{N} Q_{pq}(T)T_p(\xi)T_q(\eta), \tag{92}$$

where

$$\xi = 2X - 1 \qquad \text{and} \qquad \eta = 2Y - 1, \tag{93}$$

and T_p and T_q are the Chebyshev polynomials of degrees p and q. The derivatives appearing in the spatial operators are then evaluated as

$$Q_X = 2\sum_{p=0}^{M}\sum_{q=0}^{N} Q_{pq}^{(1,0)}T_p(\xi)T_q(\eta), \tag{94}$$

and

$$Q_Y = 2\sum_{p=0}^{M}\sum_{q=0}^{M} Q_{pq}^{(0,1)}T_p(\xi)T_q(\eta). \tag{95}$$

The Chebyshev coefficients of the X-derivative are denoted by $Q_{pq}^{(1,0)}$. They are evaluated by the recursion formulae of Eqs. (43) and (44) for each q. The Y-derivative is handled in a similar fashion.

Spectral methods for all but constant-coefficient, linear problems require some sort of weak filtering for stability. For the calculations presented below, the upper third of the frequency spectrum of the solution was filtered every 50 time-steps or so. Details are given in [19].

5.3. Shock Fitting

The Rankine-Hugoniot conditions are used both to determine the flow variables (P, u, v, and S) immediately upstream of the shock and to determine the shock position. Use the subscripts 1 and 2 to denote the variables on the downstream (right) and upstream (left) sides of the shock. Since all the quantities on the downstream side are prescribed, the flow variables on the upstream side follow routinely from the Rankine-Hugoniot relations. Of course these relations must be employed in a manner which accounts for the shock velocity and curvature.

A few preliminary definitions are needed for the equation which determines the shock position as a function of the computational time T. Let $\hat{N}$ be the unit normal to the shock front. Its components in the physical plane are

$$\hat{N} = \frac{(1, \partial x_s/\partial y)}{\sqrt{1 + (\partial x_s/\partial y)^2}} . \tag{96}$$

Let $\underline{u}_s$ denote the normal velocity of a point on the shock. Then

$$\underline{u}_s = u_s \hat{N} \tag{97}$$

and $x_s(Y,T)$ can be obtained by integrating with respect to T the projection of u_s onto the X-direction. If the incoming normal velocity relative to the shock is denoted by u_{rel}, then

$$u_{rel} = \underline{u}_1 \cdot \hat{N} - u_s \tag{98}$$

and the relative Mach number is

$$M_{rel} = u_{rel}/a_1 . \tag{99}$$

The present numerical method presumes that M_{rel} is always greater than 1.

The Rankine-Hugoniot relations imply that

$$P_2 = P_1 + \ln\left[\gamma M_{rel}^2 - \frac{\gamma-1}{2}\right] + \ln\left[\frac{2}{\gamma+1}\right] . \tag{100}$$

The equation for the shock acceleration is obtained by differentiating Eqs. (99) and (100) and then combining the results to obtain

$$u_{s,T} = A - \frac{a_1}{2\gamma M_{rel}}\left(P_{2,T} - P_{1,T}\right)\left(\gamma M_{rel}^2 - \frac{\gamma-1}{2}\right) - M_{rel} a_{1,T} , \tag{101}$$

where

$$A = \underline{u}_{1,T} \cdot \hat{N} + \underline{u}_1 \cdot \hat{N}_T . \tag{102}$$

The time derivatives on the right-hand-side of Eq. (101) are obtained from Eq. (85) using spectral approximations to the spatial derivatives. The shock velocity is obtained by integrating Eq. (101) with respect to T.

The collocation grid in the computational plane is fixed and uniform. Since the shock front moves to the right in the course of the calculation, the corresponding discrete grid in the physical plane is expanding. Thus, the effective resolution in the x-direction continually decreases during the evolution. Eventually the resolution of any calculation will become inadequate and the results will no longer be reliable. Fortunately, in many situations the important information can be extracted before this occurs, especially if the initial grid is taken to be a fine one.

5.4. Boundary Conditions

The correct boundary conditions at both the left and right boundaries depend upon the relative shock Mach number. If $\gamma = 1.4$ and $M_s > 2.08$, then the flow behind the shock is supersonic. In this case both boundaries are supersonic inflow boundaries and it is appropriate to prescribe all variables there. If $M_s < 2.08$, then these boundaries are subsonic inflow ones. The advisable procedure here is to base the numerical boundary conditions on the linearized characteristics of the Euler equations. At the left (subsonic) boundary the (linearized) characteristic variable corresponding to the outgoing characteristic direction is

$$R^- = P - \frac{\gamma}{a} u. \tag{103}$$

Similarly,

$$R^+ = P + \frac{\gamma}{a} u \tag{104}$$

corresponds to the outgoing characteristic direction at the right (subsonic) boundary.

A set of successful numerical boundary conditions on the left is obtained by first calculating preliminary values of all quantities at the left boundary and then incorporating the given values of S, v, and R^+ as

$$\begin{aligned} S &= S_{given} \\ v &= v_{given} \\ P + \frac{\gamma}{a} u &= R^+_{given} \\ P - \frac{\gamma}{a} u &= P_{prelim} - \frac{\gamma}{a} u_{prelim} \end{aligned} \tag{105}$$

Thus, the PDE is used to update the appropriate characteristic combination of variables at the boundary. The characteristic analysis is given in [33]. The particular numerical boundary condition was advocated in [34]. For the right boundary a similar characteristic correction procedure can be incorporated into the evaluation of the $P_{2,T}$ term in Eq. (101). This characteristic affects the shock velocity.

At the top and bottom boundaries (which have been stretched to infinity in the physical plane) zero disturbance boundary conditions are enforced. This is certainly justifiable whenever the fluctuations decay rapidly in these directions. However, there will be spurious reflections from the upper and lower boundaries if the disturbances extend that far out. The spurious reflections that might emanate from these boundaries need not pose a serious problem since the decreasing resolution resulting from the shock motion already limits the useful duration of a calculation.

5.5. Shock Interaction Examples

Salas, et al. [18] used the algorithm outlined above to compute the interaction of a shock with a single vortex, a hot spot and a Karman vortex street. They also gave comparisons with results from a similar second-order finite difference method. The spectral method produced virtually identical results with only 1/7 as many grid points.

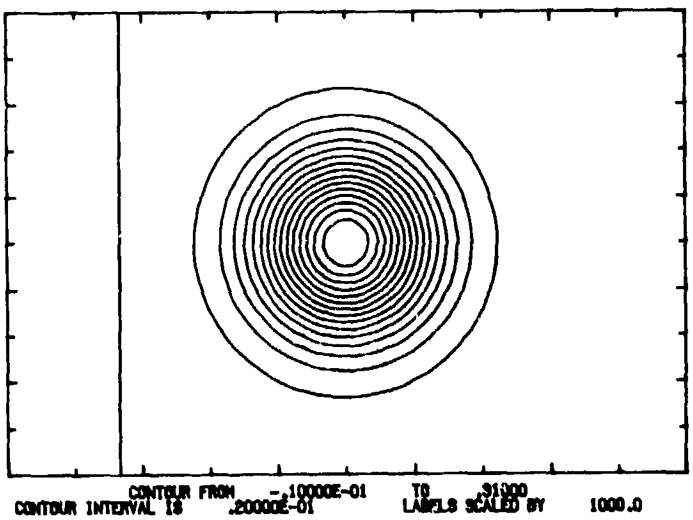

Figure 6. Initial entropy contours of a 25% hot spot about to interact with a Mach 1.2 shock.

A Mach 1.2 hot spot calculation is illustrated here in Figures 6 and 7. The hot spot situated in the quiescent field on the right in Figure 6 has the temperature distribution τ given by

$$\tau = k \exp\{-[(x-x_0)^2 + (y-y_0)^2]/2\sigma^2\}, \tag{106}$$

where $k = 0.25$, $\sigma = 1.25$, $x_0 = 0.5$ and $y_0 = 0$. The initial shock position is $x = 0$. Figure 7 displays the velocity field at time $t = 0.52$, after the shock wave has passed over the hot spot. The shock front appears a the solid line in both figures.

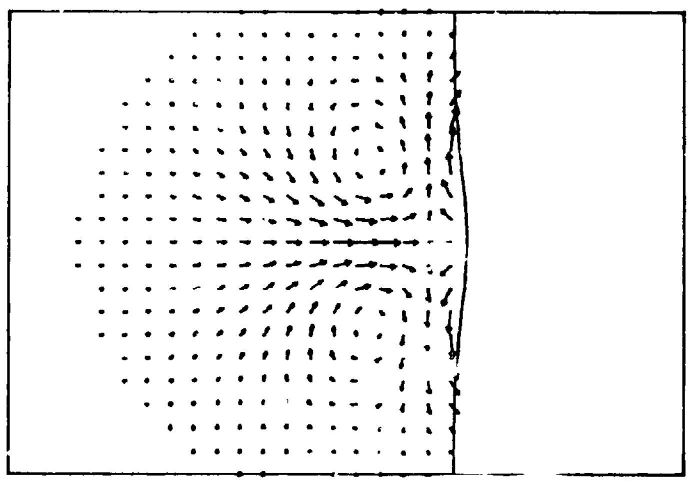

Figure 7. Perturbed upstream velocity vectors after the shock-hot spot interaction.

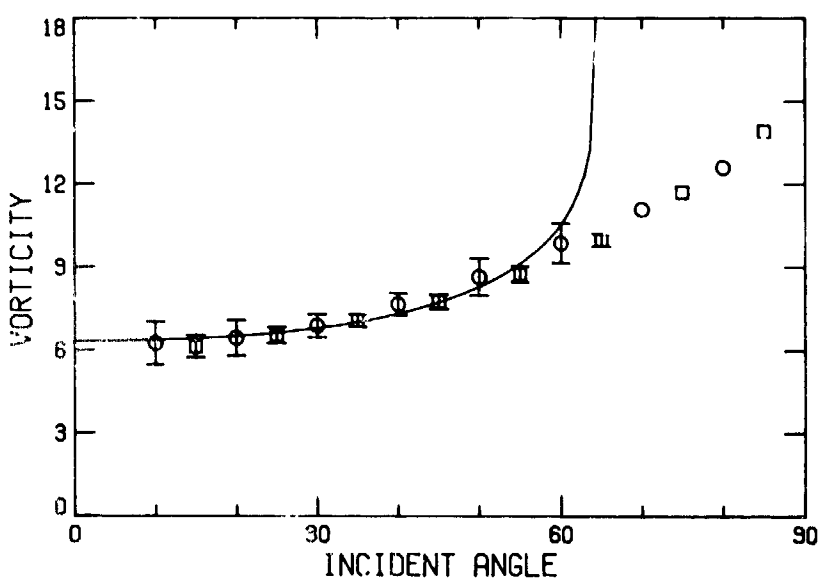

Figure 8. Spectral (circles) and finite difference (squares) results for vorticity wave amplification versus incidence angle. The solid line is the linear theory prediction.

A sample of the spectral results of Zang, et al. [30] for shock-turbulence interactions is given in Figure 8. This is a comparison of the computed, nonlinear amplification of incident Mach 3 vorticity waves with the linear theory predictions. Figure 5 shows the result of a large amplitude 30° incident vorticity wave interacting with a Mach 1.5 shock. The spectral and finite difference results are comparable even though the spectral results were produced on a far coarser grid -- 32×8 versus 64×32.

Although the present spectral calculations are more efficient than the finite difference ones in terms of storage, they do not yet offer a clear advantage in terms of machine time. The culprit is the severe explicit time-step restriction for the spectral method. A robust means of surmounting this restriction is perhaps the most pressing need for spectral methods for evolution problems.

5.6. The Blunt Body Problem

The classical problem of a blunt body in a supersonic stream has been an ideal test problem for numerical methods as it provides a relatively simple well-posed transonic problem with nontrivial initial and boundary conditions. Like most common methods the spectral method of Hussaini, et al. [19] obtains the steady state solution as the time asymptotic solution of the unsteady Euler equations which are written in the cylindrical polar coordinate (r,θ) system. The physical domain of interest consists of the known body $r = r_b(\theta)$, the unknown shock location $r = r_s(\theta,t)$, the axis of symmetry (the front stagnation streamline $\theta = \pi$) and the outflow boundary $\theta = \pi - \bar{\theta}_{max}$. For the purpose of shock fitting, the coordinate transformation

$$X = \frac{r - r_b(\theta)}{r_s(\theta,t) - r_b(\theta)}$$
$$Y = \frac{\pi - \theta}{\bar{\theta}_{max}} \tag{107}$$

is introduced so that the shock wave and the body are coordinate lines in the transformed domain. The transformed equations of motion, in the notation of the previous problem, are

$$Q_T + B\,Q_X + C\,Q_Y + R = 0, \tag{108}$$

where

$$B = \begin{bmatrix} U & \gamma X_r & (\gamma/r)X_\theta & 0 \\ (a^2/\gamma)X_r & U & 0 & 0 \\ (a^2/\gamma)(1/r)X_\theta & 0 & U & 0 \\ 0 & 0 & 0 & U \end{bmatrix}, \tag{109}$$

$$C = \begin{bmatrix} V & \gamma Y_r & (\gamma/r)Y_\theta & 0 \\ (a^2/\gamma)Y_r & V & 0 & 0 \\ (a^2/\gamma)(1/r)Y_\theta & 0 & V & 0 \\ 0 & 0 & 0 & V \end{bmatrix}, \qquad (110)$$

and

$$R = \left[\gamma \frac{u}{r}, -\frac{v^2}{r}, \frac{uv}{r}, 0\right] \qquad (111)$$

with

$$U = X_t + uX_r + \frac{v}{r} X_\theta$$
$$V = \frac{v}{r} Y_\theta. \qquad (112)$$

The flow field variables are expanded in double Chebyshev series, and the solution technique is the same as for the previous problem.

The shock boundary $r = r_s(\theta,t)$ (i.e., $X = 1$) is computed using Rankine-Hugoniot jump conditions and the compatibility equation along the incoming characteristic from the high pressure side of the shock. At the symmetry line $\theta = \pi$ $(Y = 0)$ the θ-component of velocity v is set equal to zero. On the body $r = r_b(\theta)$ (i.e., $X = 0$), the normal component of velocity u is zero. $\overline{\theta}_{max}$ is chosen so that the outflow boundary $Y = 1$ is supersonic, and hence no boundary conditions need be imposed.

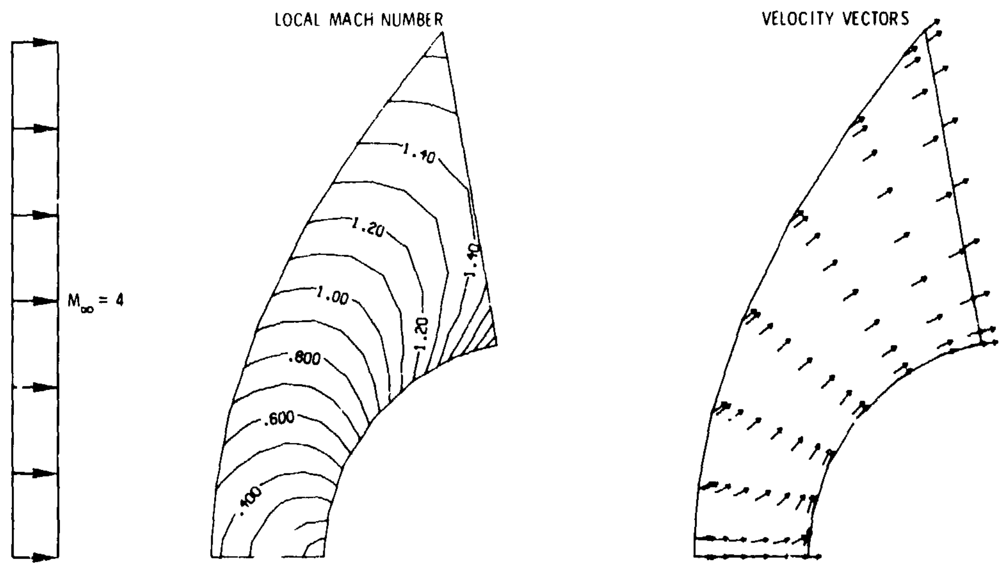

Figure 9. Spectral solution on an 8 × 8 grid for a circular cylinder in a Mach 4 uniform stream.

Figure 9 shows the Mach number contours and the velocity vectors for a circular cylinder in a uniform stream at $M_\infty = 4$. The results are found to be in very good agreement with the tabulated values given in [36]. (The grid is so coarse that the contour plotter produces jagged lines.) Figure 10 gives the results from the linearly-sheared stream. Even on a very coarse grid the spectral method captures the recirculating region.

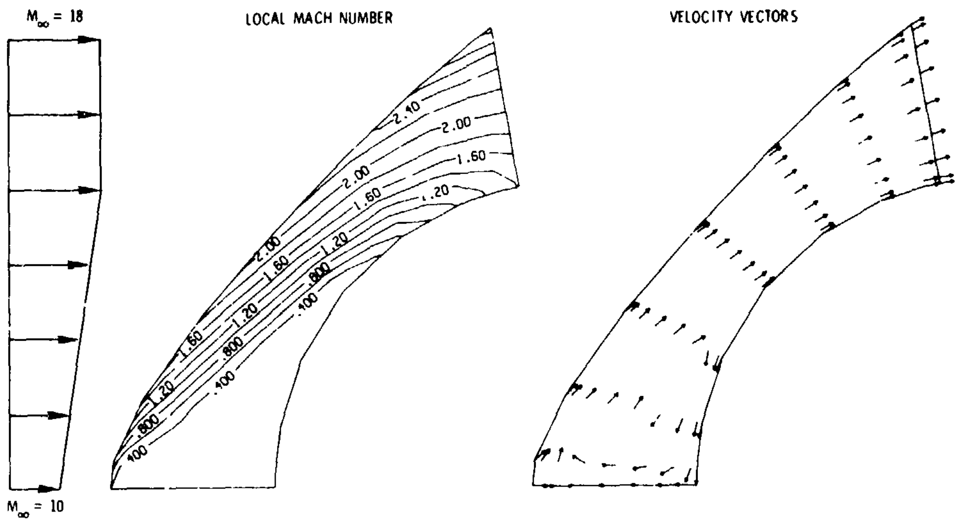

Figure 10. Spectral solution on an 8 × 8 grid for a circular cylinder in a linearly-sheared stream.

The explicit time-step restriction is a problem here as well, for neither spectral solution was run to a truly acceptable steady-state.

6. SUMMARY

Techniques are now available for obtaining viable spectral solutions to some compressible flow problems on grids far coarser than those needed for comparable finite difference solutions. The greatest success for shock-capturing spectral methods has been for potential flow. Far more sophisticated filtering techniques than are presently available appear necessary for successful shock-capturing in the context of the Euler equations. However, when the shock is fit rather than captured, the Euler solutions contain no discontinuities and thus spectral solutions might be expected to yield exponential convergence.

References

1. GOTTLIEB, D. and ORSZAG, S. - Numerical Analysis of Spectral Methods: Theory and Applications. CBMS-NSF Regional Conference Series in Applied Mathematics, Society for Industrial and Applied Mathematics, 1977.

2. SILBERMAN, I. - Planetary Waves in the Atmosphere. J. Meteor., Vol. 11, pp. 27-34, 1954.

3. ELLSAESSER, H. W. - Evaluation of Spectral Versus Grid Methods of Hemispheric Numerical Weather Prediction. J. Appl. Meteor., Vol. 5, pp. 246-262, 1966.

4. ORSZAG, S. A. - Numerical Methods for the Simulation of Turbulence. Phys. Fluids, Supplement II, Vol. 12, pp. 250-257, 1969.

5. ORSZAG, S. A. - Numerical Simulation of Incompressible Flows Within Simple Boundaries: I. Galerkin (Spectral) Representations. Stud. Appl. Math., Vol. 50, pp. 293-327, 1971.

6. ELIASEN, E., MACHENAUER, B., and RASMUSSEN, E. - On a Numerical Method for Integration of the Hydrodynamical Equations with a Spectral Representation of the Horizontal Fields. Report No. 2, Department of Meteorology, Copenhagen University, Denmark, 1970.

7. ORSZAG, S. A. and PATTERSON, G. S. - Numerical Simulation of Three-Dimensional Homogeneous Isotropic Turbulence. Phys. Rev. Lett., Vol. 28, pp. 76-79, 1972.

8. LANCZOS, C. L. - Trigonometric Interpolation of Empirical and Analytic Functions. J. Math. Phys., Vol. 17, pp. 123-199, 1938.

9. ORSZAG, S. A. - Accurate Solution of the Orr-Sommerfeld Equation. J. Fluid Mech., Vol. 50, pp. 689-703, 1971.

10. ORSZAG, S. A. and KELLS, L. C. - Transition to Turbulence in Plane Poiseuille and Plane Couette Flow. J. Fluid Mech., Vol. 96, pp. 159-205, 1980.

11. KREISS, H.-O. and OLIGER, J. - Comparison of Accurate Methods for the Integration of Hyperbolic Equations. Report No. 36, Department of Computer Science, Uppsala University, Sweden, 1971; see also Tellus, Vol. 24, pp. 199-215, 1972.

12. ORSZAG, S. A. - Comparison of Pseudospectral and Spectral Approximations. Stud. Appl. Math., Vol. 51, pp. 253-259, 1972.

13. ZANG, T. A. and HUSSAINI, M. Y. - Mixed Spectral-Finite Difference Approximations for Slightly Viscous Flows, Proceedings of the Seventh International Conference on Numerical Methods in Fluid Dynamics, Ed. Reynolds, W. C. and MacCormack, R. W, Springer-Verlag, 1981.

14. GOTTLIEB, D., LUSTMAN, L. and ORSZAG, S. A. - Spectral Calculations of One-Dimensional Inviscid Compressible Flows. SIAM J. Sci. Statis. Comput, Vol. 2, pp. 296-310, 1981.

15. TAYLOR, T. D., MYERS, R. B. and ALBERT, J. H. - Pseudo-spectral Calculations of Shock Waves, Rarefaction Waves and Contact Surfaces. Comput. & Fluids, Vol. 9, pp. 469-473, 1981.

16. STREETT, C. L. - A Spectral Method for the Solution of Transonic Potential Flow About an Arbitrary Airfoil, Proceedings of the Sixth AIAA Computational Fluid Dynamics Conference, Danvers, MA, July 1983.

17. STREETT, C. L., ZANG, T. A., and HUSSAINI, M. Y. - Spectral Multigrid Methods with Applications to Transonic Potential Flow. ICASE Report No. 83-11, 1983.

18. SALAS, M. D., ZANG T. A. and HUSSAINI, M. Y. - Shock-fitted Euler Solutions to Shock-vortex Interactions, Proceedings of the Eighth International Conference on Numerical Methods in Fluid Dynamics, Ed. Krause, E., Springer-Verlag, 1982.

19. HUSSAINI, M. Y., KOPRIVA, D. A., SALAS, M. D., and ZANG, T. A. - Spectral Methods for Euler Equations, Proceedings of the Sixth AIAA Computational Fluid Dynamics Conference, Danvers, MA, July 1983.

20. BRIGHAM, E. O. - The Fast Fourier Transform, Prentice Hall, 1974.

21. HOCKNEY, R. W. - The Potential Calculation and Some Applications. Methods Comput. Phys., Vol. 9, pp. 135-211, 1970.

22. ZANG, T. A., WONG, Y. S., and HUSSAINI, M. Y. - Spectral Multigrid Methods for Elliptic Equations. J. Comput. Phys., Vol. 48, pp. 485-501, 1982.

23. ZANG, T. A., WONG, Y. S., and HUSSAINI, M. Y. - Spectral Multigrid Methods for Elliptic Equations II. NASA CR-172131, 1983.

24. MURMAN, E. M. and COLE, J. D. - Calculation of Plane Steady Transonic Flow. AIAA J., Vol. 9, pp. 114-121, 1971.

25. HALL, M. G. - Computational Fluid Dynamics - A

Revolutionary Force in Aerodynamics, Proceedings of the Fifth AIAA Computational Fluid Dynamics Conference, Palo Alto, CA, pp. 176-188, 1981.

26. HAFEZ, M. M., SOUTH, J. C., and MURMAN, E. M. - Artificial Compressibility Methods for Numerical Solution of Transonic Full Potential Equation. AIAA J., Vol. 17, pp. 838-844, 1979.

27. HOLST, T. L. - A Fast, Conservative Algorithm for Solving the Transonic Full-Potential Equation. AIAA Paper 79-1456, 1979.

28. CATHERALL, D. - Optimum Approximate Factorization Schemes for Two Dimensional Steady Potential Flows. AIAA J., Vol. 20, pp. 1057-1063, 1982.

29. JAMESON, A. - Acceleration of Transonic Potential Flow Calculations on Arbitrary Meshes by the Multiple Grid Method. AIAA Paper 79-1458, 1979.

30. ZANG, T. A., KOPRIVA, D. A. and HUSSAINI, M. Y. - Pseudospectral Calculation of Shock Turbulence Interactions, Proceedings of the Third International Conference on Numerical Methods in Laminar and Turbulent Flow, Ed. Taylor, C., Pineridge Press, 1983.

31. PAO, S. P. and SALAS, M. D. - A Numerical Study of Two-dimensional Shock Vortex Interaction. AIAA Paper 81-1205, 1981.

32. ZANG, T. A., HUSSAINI, M. Y., and BUSHNELL, D. M. - Numerical Computations of Turbulence Amplification in Shock Wave Interactions. AIAA J., to appear.

33. OLIGER, J. and SUNDSTRÖM, A. - Theoretical and Practical Aspects of Some Initial Boundary Value Problems in Fluid Dynamics. SIAM J. Appl. Math., Vol. 35, pp. 419-446, 1978.

34. GOTTLIEB, D., GUNZBURGER, M., and TURKEL, E. - On Numerical Boundary Treatment of Hyperbolic Systems for Finite Difference and Finite Element Methods. SIAM J. Numer. Anal., Vol. 19, pp. 671-682, 1982.

35. LYUBIMOV, A. N. and RUSANOV, V. V. - Gas Flows Past Blunt Bodies, (Translation of "Techeniya Gaza Okolo Tupykh Tel, Chast' II: Tablitsy Termodinamicheskikh Funktsiy," "Nauka" Press, Moscow, 1970), NASA TT F-715, February 1973.